Dual-ring focused acoustic vortices with adjustable intensity and interval via hybrid-degenerated cribriform plates

Xin-Rui Li,[1,*] Bu-Chen Ping,[1,*] Da-Jian Wu,[1,†] Xing-Feng Zhu,[1] Di-Chao Chen,[1] and Badreddine Assouar[2,‡]

[1] *Institute of Acoustics, School of Physics and Technology, Nanjing Normal University, Nanjing 210023, China*
[2] *Université de Lorraine, CNRS, Institut Jean Lamour, F-54000 Nancy, France*

(Received 4 February 2025; revised 14 April 2025; accepted 22 May 2025; published 12 June 2025)

Dual-ring acoustic vortices carrying two orbital angular momentums are anticipated to provide new perspectives and capabilities for acoustic communication and microparticle manipulation. However, the flexible generation of a high-quality dual-ring acoustic vortex is still a challenge. Here, a hybrid-degenerated cribriform plate (HDCP) is proposed to produce a dual-ring focused acoustic vortex (FAV). The HDCP comprises L sets of circular holes arranged on L counterclockwise Fresnel spiral (FS) arms. A part of these circular holes is concurrently located on M clockwise FS-arms. Their distribution regularities on the counterclockwise and clockwise FS-arms have been analytically derived to effectively tailor the dual-ring FAVs: an outer FAV with topological charge L and an inner FAV with topological charge $-M$. Furthermore, an HDCP stainless steel structure is fabricated to experimentally demonstrate the generation of a dual-ring FAV. Finally, the combined action of the outer and inner FAVs is demonstrated to be able to roll a particle along an annular trajectory. The dual-ring FAVs generated by the proposed concept of HDCPs may find potential applications in particle manipulation and acoustic communication.

DOI: 10.1103/trtp-b6cm

I. INTRODUCTION

Acoustic vortices have attracted considerable attention in the past two decades due to their potential applications in acoustic communication [1–3], acoustic imaging [4], and microparticle manipulation [5–9]. Conventional vortex beams with integer topological charges carry single-ring intensity profiles [10–12]. More recently, a dual-ring vortex has been first explored in optics due to its special properties and applications [13–17]. A dual-ring optical vortex that carries two orbital angular momenta has been reported that is able to improve the orbital angular momentum multiplexing capacity in communication [13], sort particles, and enhance imaging quality. As a counterpart, the dual-ring acoustic vortex has not yet been thoroughly studied.

Active transducer arrays have been commonly used to dynamically and flexibly generate conventional vortex beams [8,18,19]. Producing a dual-ring acoustic vortex with more intricate acoustic field distribution requires a large number of transducer elements with high-precision phase control, which is quite challenging. Recently, a Fourier-transform system composed of an acoustic metalens and an off-axis parabolic reflector was developed to generate a dual-ring perfect acoustic vortex [20]. A single-phase-modulation metasurface has also been proposed to achieve coaxial coupling between two quasiperfect ultrasonic vortices, producing an ultrasonic braided ring beam [21]. The phase units on these metasurfaces usually sit close to each other for structural compactness, which in turn degrades the performance of acoustic vortices due to the interaction of adjacent phase units. The cribriform plate is a more concise and precise option for producing the dual-ring acoustic vortex [22]. It has been reported that the mixtures of concentric vortices with different orbital angular momentums can be realized in both optics and acoustics based on the degeneracy of cribriform plates [22–25]. However, this previous research focused on the coupling between two opposite orbital angular momentum modes [25] or two vortices with a significant difference in orbital angular momentum [23,24]. Customizing a high-quality dual-ring acoustic vortex remains a challenge.

In this work, we propose and develop a hybrid-degenerated cribriform plate (HDCP) to generate dual-ring FAVs. The HDCP is composed of L sets of circular holes located on L counterclockwise Fresnel spiral (FS) arms for generating an FAV with a topological charge of L. A part of these circular holes are concurrently located on

*Xin-Rui Li and Bu-Chen Ping contributed equally to this work.
†Contact author: wudajian@njnu.edu.cn
‡Contact author: badreddine.assouar@univ-lorraine.fr

M clockwise FS-arms, which can produce an FAV with a topological charge of $-M$. We theoretically derive the distribution rule of the circular holes on the counterclockwise and clockwise FS-arms for effectively customizing the dual-ring FAVs. It is demonstrated that the intensity ratio of the inner and outer FAVs can be adjusted by changing the diameter of the circular holes on the clockwise FS-arms. We also perform a transmitted acoustic field measurement experiment to verify the generation of a dual-ring FAV through an HDCP stainless steel sample. Finally, we use the obtained dual-ring FAVs to roll a particle along an annular trajectory.

II. HYBRID-DEGENERATED CRIBRIFORM PLATE PRODUCING A DUAL-RING FOCUSED ACOUSTIC VORTEX

It is well-known that L counterclockwise FS-arms distributed uniformly in the azimuthal direction can produce an FAV with a topological charge of L [26]. Each counterclockwise FS-arm can be further replaced by N_1 circular holes [25]. The HDCP concurrently includes L counterclockwise FS-arms and M clockwise FS-arms. The position of the n_1th circular hole on the m_1th counterclockwise FS-arm can be expressed as [25]

$$r_1(n_1,m_1)=\sqrt{\left[\sqrt{r_0^2+F^2}+\left(\frac{L\theta_1}{2\pi}-(m_1-1)\right)\lambda\right]^2-F^2}\,,\qquad \theta_1(n_1,m_1)=\frac{2\pi(n_1-1)}{N_1}+\frac{2\pi(m_1-1)}{L}\,.\qquad \begin{pmatrix} n_1=1,2,\ldots,N_1\\ m_1=1,2,\ldots,L\end{pmatrix} \tag{1}$$

Here, N_2M circular holes in these N_1L circular holes are concurrently located on M clockwise FS-arms. The position of the n_2th circular hole on the m_2th clockwise FS-arm can be expressed as [25]

$$\begin{aligned} r_2(n_2,m_2)&=\sqrt{\left[\sqrt{r_0^2+F^2}-\left(\frac{M\theta_2}{2\pi}+(m_2-1)\right)\lambda\right]^2-F^2}\,,\\ \theta_2(n_2,m_2)&=-\frac{2\pi\frac{L}{M}(n_2-1)}{N_2}-\frac{2\pi(m_2-1)}{M}\,,\\ r_1&=r_2\,,\\ \theta_1&=\theta_2+2K\pi\,.\end{aligned}\qquad \begin{pmatrix} n_2=1,2,\ldots,N_2\\ m_2=1,2,\ldots,M\\ K=0,1,\ldots\end{pmatrix} \tag{2}$$

We can then obtain the following:

$$n_1=\frac{N_1(n_2-1)}{N_2}+1\,,$$
$$m_1=-\frac{L\left(\frac{L}{M}+1\right)(n_2-1)}{N_2}-\frac{L}{M}(m_2-KM-1)+1\,. \tag{3}$$

In Eq. (3), in order to ensure that both n_1 and m_1 are positive integers, N_1 should be an integer multiple of N_2, L should be an integer multiple of M, and N_2 must be a divisor of $L(L/M+1)$. When L is not an integer multiple of M, it is very difficult to construct a degenerated cribriform plate for producing the dual-ring FAVs [25].

Furthermore, n_1 and θ_1 can be rewritten as

$$n_1=N_1\left[-\frac{(m_1-1)}{L\left(\frac{L}{M}+1\right)}-\frac{(m_2-1-KM)}{M\left(\frac{L}{M}+1\right)}\right]+1\,,$$
$$\theta_1=\frac{2\pi}{M\left(\frac{L}{M}+1\right)}(m_1-m_2+KM)\,. \tag{4}$$

This means that the circular holes in L counterclockwise FS-arms satisfying Eq. (4) are concurrently located on M clockwise FS-arms and the angular interval of these circular holes is $2\pi/(L/M+1)$. For example, Fig. 1(a) shows the schematic diagram of an acoustic structure plate engraved with $12N_1$ circular holes on 12 counterclockwise FS-arms circular holes for generating a FAV with a topological charge of $l_1=L=12$, where 4 clockwise FS-arms circular holes (red holes) are included. Here, the N_2 value is set at $L(L/M+1)=48$ and then the N_1 value is also fixed at 48. To clarify the design principle, the first counterclockwise FS-arm circular holes ($m_1=1$) and the first clockwise FS-arm circular holes ($m_2=1$) are highlighted in Fig. 1(b). According to Eq. (4), in this case of $m_1=1$ and $m_2=1$, the circular holes of ($n_1=1$, $\theta_1=0$), ($n_1=13$, $\theta_1=\pi/2$), ($n_1=25$, $\theta_1=\pi$), and ($n_1=37$, $\theta_1=3\pi/2$) on the first counterclockwise FS-arm circular holes are located on the first clockwise FS-arm circular holes, as shown in Fig. 1(b). Each counterclockwise FS-arm circular hole provides 4 circular holes for the first clockwise FS-arm circular holes and 12 counterclockwise FS-arm circular holes, in total sharing 48 circular holes for constructing the first clockwise FS-arm circular holes. Figures 1(c) and 1(d) show the normalized simulated acoustic intensity and phase distributions of the transmitted acoustic fields at the focal plane of $z = 20\lambda$ when an acoustic plane wave passes through the acoustic structure plate engraved with circular holes, as shown in Fig. 1(a). Throughout this work, the embedding medium is water with a density of 1000 kg m^{-3} and a sound velocity of 1490 m s^{-1}, and the working frequency is fixed at 500 kHz (wavelength $\lambda = \sim 0.3$ cm). The finite element numerical simulations are performed using COMSOL Multiphysics software to verify our approach. The HDCP is composed of stainless steel with a density of 7900 kg m^{-3}, a longitudinal wave speed of 5240 m s^{-1}, and a shear wave speed of 2978 m s^{-1}. Its acoustic impedance is much larger than that of water [3,10] and, thus, the HDCP can be set to be acoustically rigid. In simulations, the boundaries of the HDCP are set as sound-hard boundaries. The plane wave radiation boundaries are used around the numerical models to eliminate reflected waves [6]. Here, the diameter of the circular hole is set at $d = 0.7$ mm. It is observed that the intensity profile consists of a single bright ring and the corresponding phase shift is 24π. Only the characteristics of an FAV with a topological charge of $l_1 = 12$ could be distinctly observed in Figs. 1(c) and 1(d), and the effect of the four clockwise FS-arm circular holes cannot be found in the center of the acoustic field.

It was reported that the transmissivity of a circular hole unit increases with diameter while maintaining a nearly constant phase shift [25,27]. If we increase the diameters of the circular holes on the four clockwise FS-arms to $d_2 = 2.1$ mm, as shown in Figs. 1(e) and 1(f), the contribution of the four clockwise FS-arm circular holes will be enhanced. As an acoustic plane wave passes through the HDCP, as shown in Fig. 1(e), a dual-ring intensity profile can be observed at the focal plane in Fig. 1(g), and the corresponding phase shifts of the outer and inner FAVs are 24π and -8π, as shown in Fig. 1(h). Therefore, the

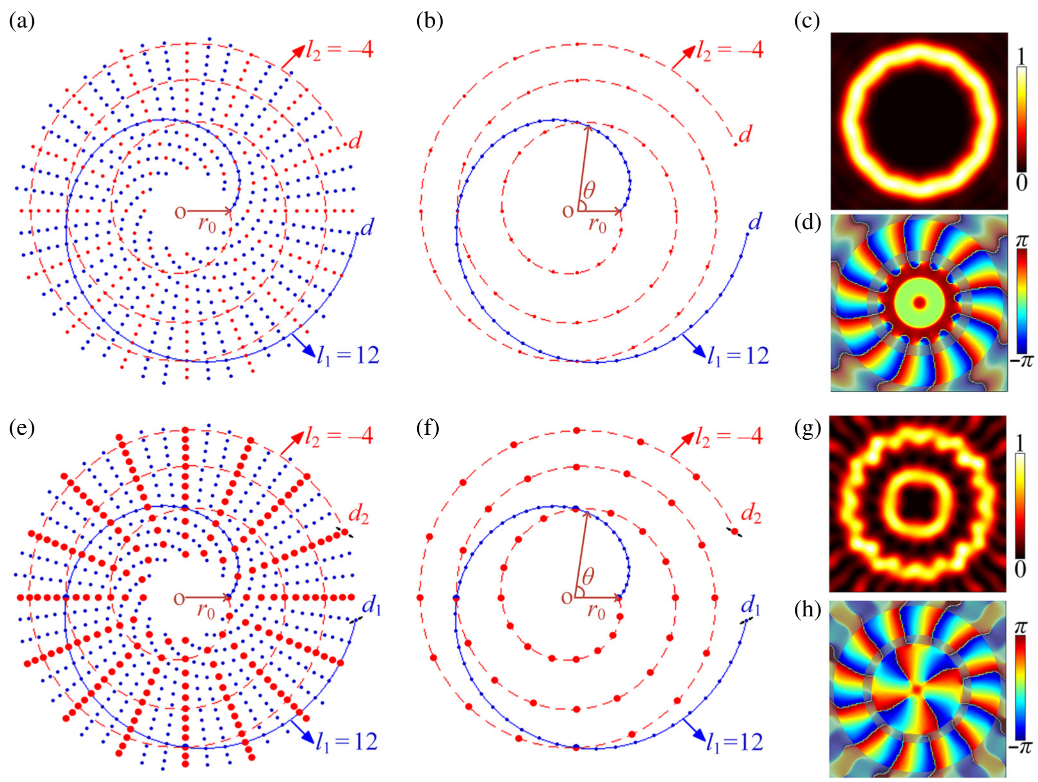

FIG. 1. (a) Schematic diagram of an acoustic structure plate engraved with 576 circular holes on 12 counterclockwise FS-arms for generating a FAV with a topological charge of $l_1 = 12$. Here, the diameter of the circular hole is set at $d = 0.7$ mm and $N_1 = N_2 = 48$. (b) First counterclockwise FS-arm circular holes (blue circular holes) for $l_1 = 12$ and first clockwise FS-arm circular holes (red circular holes) for $l_2 = -4$. Corresponding (c) normalized simulated acoustic intensity and (d) phase distributions of the transmitted acoustic fields at the focal plane of $z = 20\lambda$ as an acoustic plane wave passes through the acoustic structure plate. (e) Schematic diagram of an HDCP including 12 counterclockwise FS-arms circular holes with a diameter of $d_1 = 0.7$ mm and 4 clockwise FS-arms circular holes with a diameter of $d_2 = 2.1$ mm for generating a dual-ring focused acoustic vortex with topological charges of $l_1 = 12$ and $l_2 = -4$. (f) First counterclockwise FS-arm circular holes (blue circular holes) for $l_1 = 12$ and first clockwise FS-arm circular holes (red circular holes) for $l_2 = -4$. Corresponding (g) normalized simulated acoustic intensity and (h) phase distributions of the transmitted acoustic fields at the focal plane of $z = 20\lambda$. The work frequency is 500 kHz and the embedding medium is water.

proposed HDCP can generate a dual-ring FAV with topological charges of $l_1 = 12$ and $l_2 = -4$. In addition, we should note that a well-designed HDCP can also generate a dual-ring FAV with two topological charges of the same sign (Appendix). A triple-ring FAV with three topological charges can also be obtained using a similar mechanism (Appendix).

III. RESULTS AND DISCUSSION

We first investigated the variations in the transmitted acoustic field with the size of the red circular holes on the four clockwise FS-arms. Figures 2(a1)–2(a4) show the normalized simulated acoustic intensity distributions of the transmitted acoustic fields produced by the HDCPs with (a1) $d_2 = 0.7$ mm, (a2) $d_2 = 1.4$ mm, (a3) $d_2 = 2.1$ mm, and (a4) $d_2 = 2.8$ mm at the focal plane of $z = 20\lambda$. Here, $N_1 = N_2 = 48$, $d_1 = 0.7$ mm, $l_1 = 12$, and $l_2 = -4$.

Figures 2(b1)–2(b4) display acoustic intensity profiles along the white dashed lines I, II, III, and IV in Figs. 2(a1)–2(a4). Corresponding simulated phase distributions of the transmitted acoustic fields are shown in Figs. 2(c1)–2(c4). As $d_1 = d_2 = 0.7$ mm, the intensity profile exhibits a single FAV with $l_1 = 12$ (a phase shift of 24π). In Fig. 2(b1), the normalized intensity along line I reaches its maximum of ∼0.018 at a radius of $w_1 = \sim 3.15\lambda$. As d_2 increases to 1.4 mm, it is found that, in addition to the outer bright ring with enhanced intensity, a small ring appears in the central region of the intensity profile in Fig. 2(a2). The maximal normalized intensity of the outer and inner rings along the line II reach ∼0.094 and ∼0.037 at radii of $w_1 = \sim 3.05\lambda$ and $w_2 = \sim 1.25\lambda$, respectively, as shown in Fig. 2(b2). In the phase distribution, the phase shifts of the outer and inner FAVs are 24π and -8π, respectively, which demonstrates the topological charges of a dual-ring FAV are $l_1 = 12$ and $l_2 = -4$. As the d_2 value further increases to 2.1 mm, the intensity of the inner ring is rapidly enhanced, while that of the outer ring also rises gradually. The maximal normalized intensity of the outer and inner rings along line III achieve ∼0.35 and ∼0.3, respectively, as illustrated in Fig. 2(b3). In Fig. 2(c3), the phase shifts of the outer and inner FAVs are also 24π and -8π. For $d_2 = 2.8$ mm, the intensities of both the inner and outer FAVs are enhanced and the intensity of the inner FAV is distinctly higher than that of the outer FAV, as shown in Figs. 2(a4) and 2(b4). The phase profile in Fig. 2(c4) remains unchanged. Therefore, the intensity of the outer and inner FAVs of a dual-ring FAV can be effectively enhanced by increasing the diameters of the circular holes

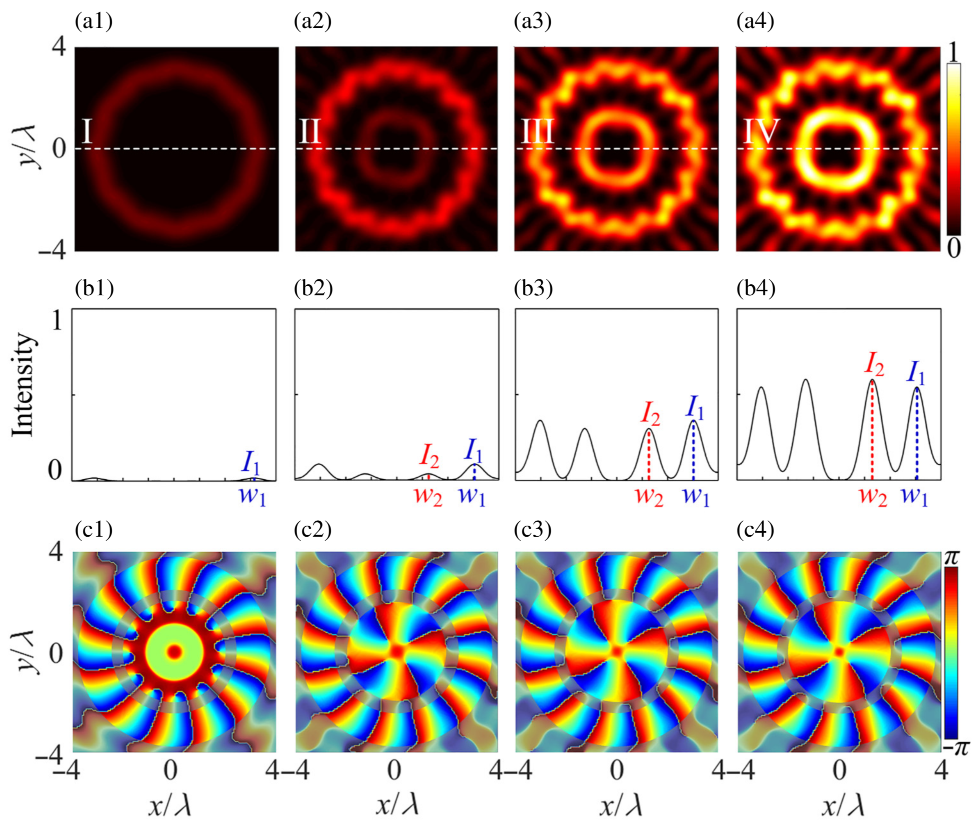

FIG. 2. Normalized simulated acoustic intensity distributions of the transmitted acoustic fields produced by HDCPs with (a1) $d_2 = 0.7$ mm, (a2) $d_2 = 1.4$ mm, (a3) $d_2 = 2.1$ mm, and (a4) $d_2 = 2.8$ mm at the focal plane of $z = 20\lambda$. Here, $N_1 = N_2 = 48$, $d_1 = 0.7$ mm, $l_1 = 12$, and $l_2 = -4$. (b1)–(b4) Acoustic intensity profiles along the white dashed lines I, II, III, and IV in (a1)–(a4). (c1)–(c4) Corresponding simulated phase distributions of the transmitted acoustic fields.

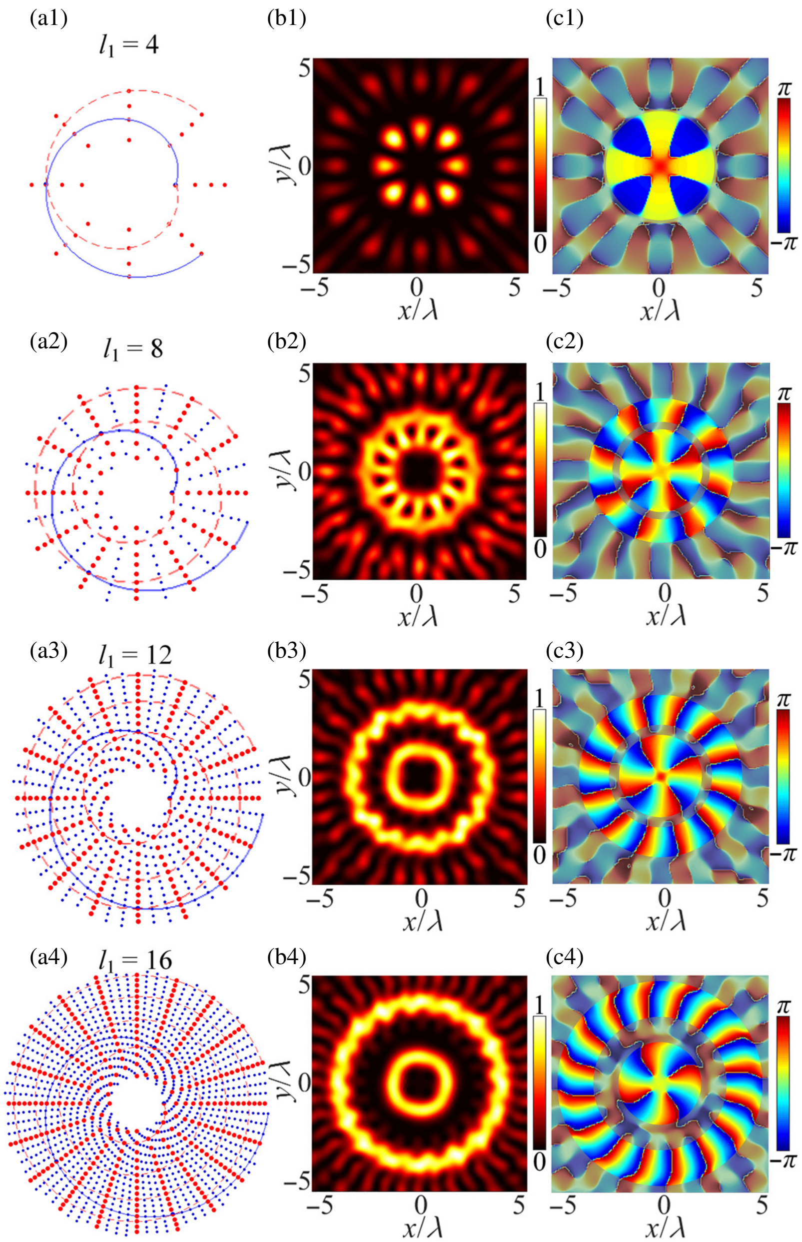

FIG. 3. Schematic diagrams of HDCPs for generating dual-ring FAVs with topological charges of (a1) $l_1 = 4$, $l_2 = -4$, and $N_1 = N_2 = 8$, (a2) $l_1 = 8$, $l_2 = -4$, and $N_1 = N_2 = 24$, (a3) $l_1 = 12$, $l_2 = -4$, and $N_1 = N_2 = 48$, and (a4) $l_1 = 16$, $l_2 = -4$, and $N_1 = N_2 = 80$. Here, d_1 and d_2 are 0.7 mm and 2.1 mm, respectively. Corresponding (b1)–(b4) normalized simulated acoustic intensity and (c1)–(c4) phase distributions of the transmitted acoustic fields at the focal plane of $z = 20\lambda$.

on the four clockwise FS-arms while the phase profile stays constant. Moreover, the intensity of the inner FAV exhibits a more rapid growth rate compared with that of the outer FAV. Thus, by changing the d_2 value, the intensity of the dual-ring FAVs can be effectively modulated.

Furthermore, we have investigated the evolutionary process of dual-ring FAVs in response to variations in the topological charge. As discussed in Eq. (3), $L = l_1$ must be an integer multiple of $M = -l_2$, N_1 should be an integer multiple of N_2, and N_2 must be a divisor of $L(L/M + 1)$. If $M = 4$, L can be chosen as 4, 8, 12, 16, etc. In Fig. 3, the first column shows the schematic diagrams of HDCPs for generating dual-ring FAVs with topological charges of (a1) $l_1 = 4$, $l_2 = -4$, and $N_1 = N_2 = 8$, (a2) $l_1 = 8$, $l_2 = -4$, and $N_1 = N_2 = 24$, (a3) $l_1 = 12$, $l_2 = -4$, and $N_1 = N_2 = 48$, and (a4) $l_1 = 16$, $l_2 = -4$, and $N_1 = N_2 = 80$. Here, d_1 and d_2 are 0.7 mm and 2.1 mm, respectively. Figures 3(b1)–3(b4) show the normalized simulated acoustic intensity distributions of the transmitted acoustic fields produced by HDCPs at the focal plane of $z = 20\lambda$. The corresponding simulated phase distributions of the transmitted acoustic fields are shown in Fig. 3(c1)–3(c4). In Fig. 3(a1), the HDCP includes 32 completely degenerate circular holes, which simultaneously construct the 4 counterclockwise FS-arms and 4 clockwise FS-arms. In this case, 32 circular holes located on the 4 counterclockwise FS-arms are completely overlapping with 32 circular holes on the 4 clockwise FS-arms.

When an acoustic plane wave passes through this HDCP, two FAVs with topological charges of $l_1 = 4$ and $l_2 = -4$ are produced at the focal plane of $z = 20\lambda$ and the coupling between them results in the 8 petallike bright spots, as shown in Fig. 3(b1). Here, the diameters of the circular holes are fixed at 2.1 mm. The phase profile in Fig. 3(c1) is divided into 8 sections and the adjacent phase jump is π. These features effectively match those in a previous report [25]. In Fig. 3(a2), the HDCP contains 192 circular holes with a diameter of $d_1 = 0.7$ mm on 8 counterclockwise FS-arms for generating a FAV with a topological charge of $l_1 = 8$, where 96 circular holes on 4 clockwise FS-arms are replaced by larger circular holes with a diameter of $d_2 = 2.1$ mm for generating a FAV with a topological charge of $l_2 = -4$. It is observed in Fig. 3(b2) that the radius of the outer bright ring increases with the l_1 value and a wagon wheel pattern can be obtained at the focal plane due to the coupling between two FAVs with topological charges of $l_1 = 8$ and $l_2 = -4$. Here, 12 dark spots are evenly distributed on a circle with a radius of $\sim 2\lambda$ in the acoustic intensity distribution. The phase shifts of the outer and inner FAVs are 16π and -8π, as shown in Fig. 3(c2). As the l_1 value increases to 12, the radius of the outer FAV with $l_1 = 12$ further increases and that of the inner FAV is unchanged. The coupling between two FAVs becomes very weak and a dual-ring intensity profile is presented in Fig. 3(b3). In Fig. 3(c3), the phase shifts of the outer and inner FAVs are 24π and -8π, respectively. Finally, as the l_1 value further increases to 16, the number N_1 of circular holes on each 16 counterclockwise FS-arm increases to 80. The circular holes of $(n_1 = 1, \theta_1 = 0)$, $(n_1 = 17, \theta_1 = 2\pi/5)$, $(n_1 = 33,\ \theta_1 = 4\pi/5)$, $(n_1 = 49,\ \theta_1 = 6\pi/5)$, and $(n_1 = 65,\ \theta_1 = 8\pi/5)$ on the first counterclockwise FS-arm circular holes are located on the first clockwise FS-arm circular holes, as shown in Fig. 3(a4). Figure 3(b4) shows an outer bright intensity ring with a larger radius and the interval between two bright intensity rings is further enlarged. The phase shifts of the outer and inner FAVs are 32π and -8π, respectively, as shown in Fig. 3(c4). Therefore, the interval of the dual-ring FAVs produced by the proposed HDCP can be adjusted by modulating the topological charges of the dual-ring FAVs.

IV. EXPERIMENTAL DEMONSTRATION

An HDCP stainless steel structure is fabricated using a laser engraving technique to experimentally verify the generation of a dual-ring FAV. Figure 4(a) shows the schematic diagram of the experimental setup of the transmitted acoustic field measurement.

Figure 4(b) is a photograph of the HDCP stainless steel structure for generating a dual-ring FAV with the topological charges of $l_1 = 12$ and $l_2 = -4$. Here, d_1 and d_2 are 0.7 mm and 2.1 mm, respectively, and $N_1 = N_2 = 48$. The stainless steel plate had a density of 7900 kg m^{-3}, a longitudinal wave speed of 5240 m s^{-1}, and a shear wave speed of 2978 m s^{-1}; thus, its acoustic impedance is much larger than that of water [28,29]. To match the size of the existing ultrasound transducer, the focal plane of the HDCP stainless steel structure is adjusted to $z = 5\lambda$. In this case, the effective region of the HDCP stainless steel structure is reduced to a circular area with a diameter of $\sim 35\lambda$ ($\sim$10.5 cm). During the measurement of the transmitted acoustic field, an ultrasound transducer (placed at the back of the HDCP stainless steel sample) emits an incident acoustic plane wave with a frequency of 500 kHz. A needle hydrophone (PA NH0500) is connected with an *x*–*y*–*z* stepper motor to measure the transmitted acoustic field on the focal plane of $\sim 5\lambda$ with a step size of 0.3 mm ($\sim 0.1\lambda$). Figures 4(c) and 4(d) show the simulated normalized acoustic intensity and phase distributions of the transmitted acoustic fields through the HDCP on the focal plane of $z = 5\lambda$. The top and bottom panels in Fig. 4(e) display the normalized simulated and measured acoustic intensity distributions in the measurement area indicated by the white dashed box in Fig. 4(c). The top and bottom panels in Fig. 4(f) show the simulated and measured acoustic phase distributions in the measurement area. The measured results are further compared with the simulations (Appendix). The simulated and measured results exhibit good agreement, although there are some slight deviations. These deviations may arise from fabrication imperfections in the structure, as well as the inherent limitations in the precision of the experimental system. Additionally, we examine the manner in which the dual-ring FAVs generated via the HDCP perform particle manipulation. Figures 4(g) and 4(h) show the simulated acoustic energy flow density (white arrows) of the dual-ring FAVs produced by the HDCP at the focal plane of $z = 5\lambda$. It is observed that the acoustic energy flow density of the inner and outer FAVs possesses opposite directions. Moreover, it is observed in Fig. 4(h) that the direction of the phase gradient in the gap between the inner and outer FAVs is clockwise. This phase gradient is an in-plane component of the radiation force, which can provide a driving force to push the particle along its direction of travel [20,30]. Therefore, when a particle with a suitable size is trapped between the inner and outer FAVs, it will roll clockwise because of the clockwise phase gradient and the opposite direction of the acoustic energy flow density. Finally, we demonstrate the particle rolling due to the dual-ring FAVs produced by the HDCP structure. Figure 4(i) shows the schematic diagram of the experimental setup of particle rolling. In this experiment, an ultrasound transducer with a frequency of 500 kHz is under the HDCP stainless steel structure, and the focal plane of the dual-ring FAVs produced by the HDCP structure is formed at the water-air interface. A polypropylene particle floating on the water surface is introduced into the focal plane of the dual-ring

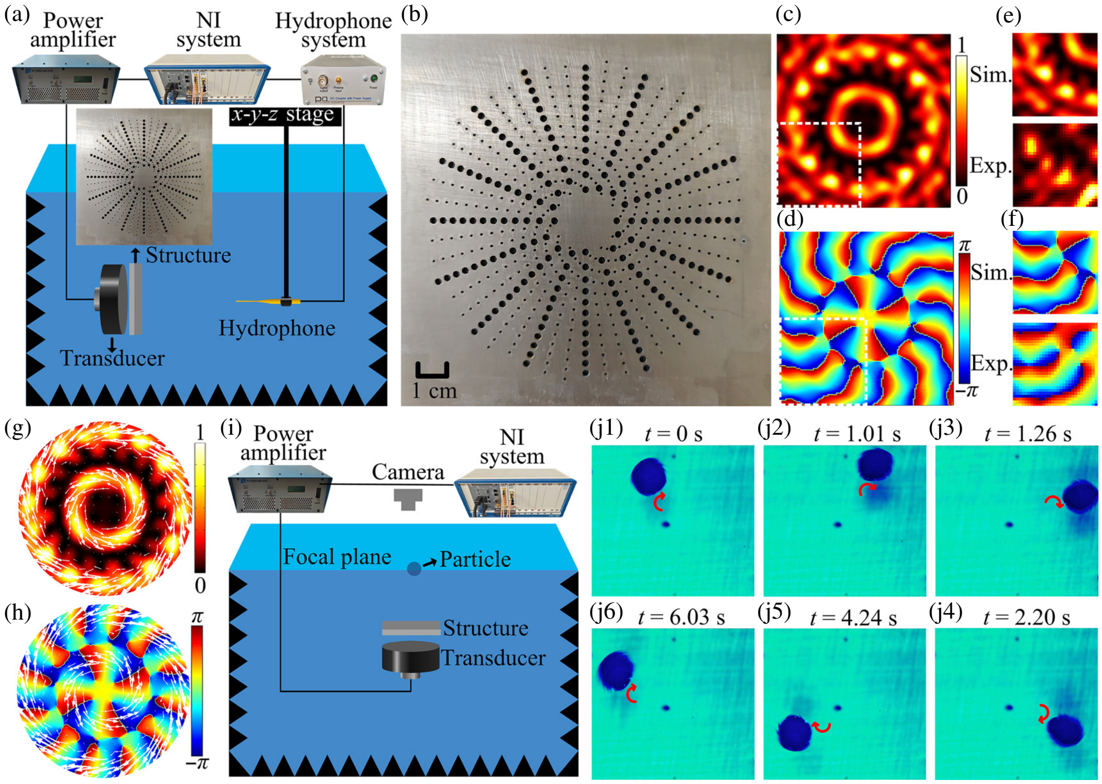

FIG. 4. (a) Schematic diagram of the experimental setup of the transmitted acoustic field measurement. (b) Photograph of an HDCP stainless steel sample for generating dual-ring FAVs with topological charges of $l_1 = 12$ and $l_2 = -4$. Here, d_1 and d_2 are 0.7 mm and 2.1 mm, respectively, and $N_1 = N_2 = 48$. (c) Normalized simulated acoustic intensity and (d) phase distributions of the transmitted acoustic fields through the HDCP on the focal plane of $z = 5\lambda$. The top and bottom panels of (e) show the normalized simulated and measured acoustic intensity distributions in the measurement area indicated by the white dashed box in (c). The top and bottom panels of (f) show the simulated and measured acoustic phase distributions in the measurement area. (g),(h) Simulated acoustic energy flow density (white arrows) of the dual-ring FAVs produced by the HDCP stainless steel sample at the focal plane of $z = 5\lambda$. (i) Schematic diagram of the experimental setup of particle rolling. (j1)–(j6) Six time-sequential photographs showing the rolling trajectory of a polypropylene particle driven by the dual-ring FAVs. The diameter of the polypropylene particle is $\sim\lambda$.

FAVs. The diameter of the particle is $\sim\lambda$. The longitudinal speed, shear speed, and density of the polypropylene particle are 2650 m s^{-1}, 1300 m s^{-1}, and 913 kg m^{-3} [31], respectively. One digital camera is mounted onto the top of the entire experiment system to record the movement of the polypropylene particle. Figures 4(j1)–4(j6) display six time-sequential photographs showing the rolling trajectory of a polypropylene particle driven by the dual-ring FAVs. The total movement of the particle can be seen in Video 1. It is observed that the polypropylene particle trapped between the inner and outer FAVs rolls along the annular trajectory in a clockwise direction.

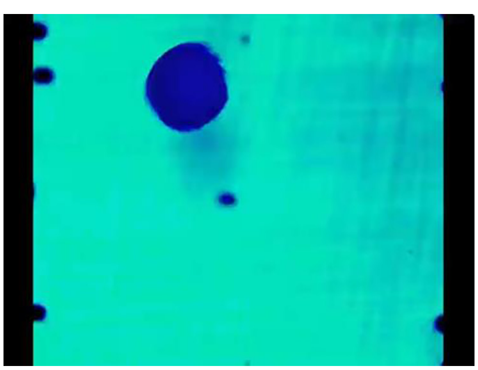

VIDEO 1. Visualization of the total movement of the polypropylene particle.

V. CONCLUSION

A hybrid-degenerated cribriform plate has been conceived to generate a dual-ring FAV. It includes N_1L circular holes with a diameter of d_1 located on L counterclockwise FS-arms for generating an outer FAV with a topological charge of L. Furthermore, N_2M of these circular holes are concurrently located on M clockwise FS-arms, which produces an inner FAV with a topological charge of $-M$. We have derived the theoretical distribution regularities of the circular holes on the counterclockwise and clockwise FS-arms and found that N_1 should be an integer multiple of N_2, L should be an integer multiple of M, and N_2 must be a divisor of $L(L/M+1)$. We have demonstrated that the intensity ratio of the inner and outer FAVs can be adjusted by varying the diameter of the circular holes on the clockwise FS-arms. Moreover, the interval of the inner and outer FAVs can be enlarged by increasing the value L/M. Finally, we have experimentally demonstrated that the HDCP stainless steel structure is capable of producing a dual-ring FAV, which has the ability to roll a particle along an annular trajectory.

To date, a significant amount of research has been dedicated to exploring the generation of ultrasonic vortices and their applications. The possibility of producing complex ultrasonic vortices has been demonstrated using phase plates [7,21]. However, challenges arise when adjusting the amplitude of the acoustic waves, while the nonlocality of the acoustic field can significantly impact the efficiency of the phase plates. Acoustic structure plates, such as coiling slits and discrete spiral structure plates, have the advantages of lightweight size and thinner thickness in generating ultrasonic vortices [10,26]. Creating dual-ring ultrasonic vortices through existing structure plates is challenging because of design and manufacturing constraints.

In this work, we propose an HDCP that effectively generates dual-ring FAVs with an adjustable intensity and interval. This can be achieved by adjusting the size of the circular holes on the clockwise or counterclockwise FS-arms and modulating the topological charges of the dual-ring focused ultrasonic vortices. The HDCP offers a simplified and more effective method for generating dual-ring and even triple-ring focused ultrasonic vortices, overcoming some of the drawbacks of traditional approaches.

ACKNOWLEDGMENTS

This work was supported by the National Natural Science Foundation of China (Grants No. 12374439, No. 12404531, No. 12474455, and No. 12027808).

DATA AVAILABILITY

The data that support the findings of this article are not publicly available. The data are available from the authors upon reasonable request.

APPENDIX

If the topological charges of the dual-ring FAVs have the same sign, the distribution rule of the circular holes on the HDCP should be rederived. For example, if the topological charges $l_1 = L$ and $l_2 = M$ are both positive, the HDCP must concurrently include L counterclockwise FS-arms and M counterclockwise FS-arms. The position of the n_1th circular hole on the m_1th counterclockwise FS-arm can be expressed as

$$\begin{aligned} r_1(n_1,m_1) &= \sqrt{\left[\sqrt{r_0^2+F^2}+\left(\frac{L\theta_1}{2\pi}-(m_1-1)\right)\lambda\right]^2-F^2}\ , \\ \theta_1(n_1,m_1) &= \frac{2\pi(n_1-1)}{N_1}+\frac{2\pi(m_1-1)}{L}\ . \end{aligned} \quad \begin{pmatrix} n_1=1,2,\ldots,N_1 \\ m_1=1,2,\ldots,L \end{pmatrix} \tag{A1}$$

The position of the n_2th circular hole on the m_2th counterclockwise FS-arm can be given as

$$\begin{aligned} r_2(n_2,m_2) &= \sqrt{\left[\sqrt{r_0^2+F^2}+\left(\frac{M\theta_2}{2\pi}-(m_2-1)\right)\lambda\right]^2-F^2}\ , \\ \theta_2(n_2,m_2) &= \frac{2\pi\frac{L}{M}(n_2-1)}{N_2}+\frac{2\pi(m_2-1)}{M}\ , \\ r_1 &= r_2\ , \\ \theta_1 &= \theta_2\ . \end{aligned} \quad \begin{pmatrix} n_2=1,2,\ldots,N_2 \\ m_2=1,2,\ldots,M \end{pmatrix} \tag{A2}$$

We can then obtain the following:

$$\begin{aligned} n_1 &= \frac{N_1(n_2-1)}{N_2}+1\ , \\ m_1 &= \frac{L\left(\frac{L}{M}-1\right)(n_2-1)}{N_2}+\frac{L}{M}(m_2-1)+1\ . \end{aligned} \tag{A3}$$

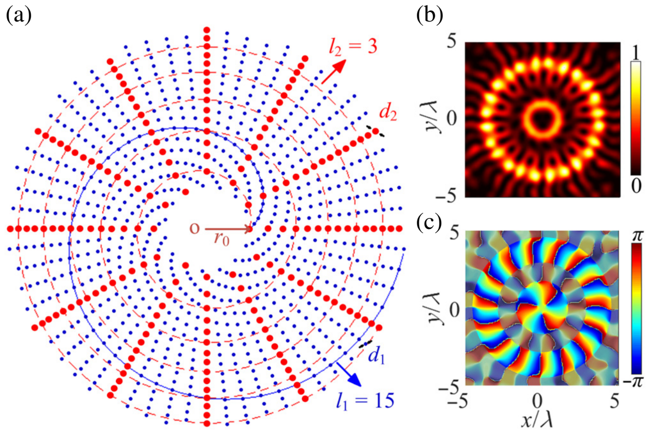

FIG. 5. (a) Schematic diagram of an HDCP including 15 counterclockwise FS-arms circular holes with a diameter of $d_1 = 0.7$ mm and 3 counterclockwise FS-arms circular holes with a diameter of $d_2 = 2.1$ mm for generating a dual-ring FAV with topological charges of $l_1 = 15$ and $l_2 = 3$. Corresponding (b) normalized simulated acoustic intensity and (c) phase distributions of the transmitted acoustic fields at the focal plane of $z = 20\lambda$. The work frequency is 500 kHz and the embedding medium is water.

Therefore, N_1 should be an integer multiple of N_2 and N_2 must be a divisor of $L(L/M - 1)$.

Figure 5(a) shows the schematic diagram of an HDCP for generating a dual-ring FAV with topological charges of $l_1 = 15$ and $l_2 = 3$. Here, d_1 and d_2 are 0.7 mm and 2.1 mm, respectively. Figures 5(b) and 5(c) display the normalized simulated acoustic intensity and phase distributions of the transmitted acoustic fields generated by an HDCP at the focal plane of $z = 20\lambda$. In Fig. 5(a), the HDCP contains $15N_1$ circular holes (blue holes) with a diameter of $d_1 = 0.7$ mm on 15 counterclockwise FS-arms for generating an FAV with a topological charge of $l_1 = 15$, where $3N_2$ circular holes (red holes) on 3 counterclockwise FS-arms are replaced by circular holes with a diameter of $d_2 = 2.1$ mm for generating a FAV with a topological charge of $l_2 = 3$. Here, the N_2 value is set at $L(L/M - 1) = 60$ and then the N_1 value is also fixed at 60. In Fig. 5(b), a dual-ring intensity profile can be observed at the focal plane. The phase shifts of the outer and inner FAVs are 30π and 6π, respectively, as shown in Fig. 5(c). Therefore, the proposed HDCP can generate a dual-ring FAV with two topological charges of the same sign.

We also explore the realization of a triple-ring FAV by the proposed HDCP. In order to produce a triple-ring FAV with topological charges of $l_1 = L$, $l_2 = M$, and $l_3 = -Q$, the HDCP should concurrently include L counterclockwise FS-arms, M counterclockwise FS-arms, and Q clockwise FS-arms. The positions of the circular holes on the L counterclockwise FS-arms and on the M counterclockwise FS-arms can be obtained via Eqs. (A1) and (A2), respectively. For the third FAV with a topological charge of $l_3 = -Q$, the position of the n_3th circular hole on the m_3th clockwise FS-arm can be expressed as

$$r_3(n_3, m_3) = \sqrt{\left[\sqrt{r_0^2 + F^2} - \left(\frac{Q\theta_3}{2\pi} + (m_3 - 1)\right)\lambda\right]^2 - F^2}, \quad \theta_3(n_3, m_3) = -\frac{2\pi\frac{L}{Q}(n_3 - 1)}{N_3} - \frac{2\pi(m_3 - 1)}{Q}. \quad \begin{pmatrix} n_3 = 1, 2, \ldots, N_3 \\ m_3 = 1, 2, \ldots, Q \end{pmatrix} \tag{A4}$$

Here, L is an integer multiple of M and Q is also an integer multiple of M; N_1 should be an integer multiple of N_2, N_2 must be a divisor of $L(L/M - 1)$, and N_3 should be an integer multiple of N_2.

Figure 6(a) shows a schematic diagram of an HDCP for generating a triple-ring FAV with $l_1 = 20$, $l_2 = 4$, and $l_3 = -12$. Here, d_1, d_2, and d_3 are 0.7 mm, 2.1 mm, and 0.7 mm, respectively. Figures 6(b) and 6(c) represent the normalized simulated acoustic intensity and phase distributions of the transmitted acoustic fields generated by the HDCP at the focal plane of $z = 20\lambda$. In Fig. 6(a), the HDCP contains 1600 circular holes (blue holes) with a diameter of $d_1 = 0.7$ mm on 20 counterclockwise FS-arms for generating a FAV with $l_1 = 20$ and 960 circular holes (black holes) with a diameter of $d_3 = 0.7$ mm on 12 clockwise FS-arms for generating a FAV with $l_3 = -12$, where 320 circular holes (red holes) on 4 counterclockwise FS-arms are replaced by larger circular holes with a diameter of $d_2 = 2.1$ mm for generating a FAV with $l_2 = 4$. When an acoustic plane wave transmits through this HDCP, a triple-ring intensity profile can be observed, as seen in Fig. 6(b). The corresponding phase shifts of the outer, middle, and inner FAVs are 40π, -24π, and 8π, respectively, as shown in Fig. 6(c).

Figures 7(a1) and 7(b1) show normalized simulated and measured acoustic intensity distributions in the measurement area, respectively. Figures 7(a2) and 7(b2) illustrate the corresponding simulated and measured phase

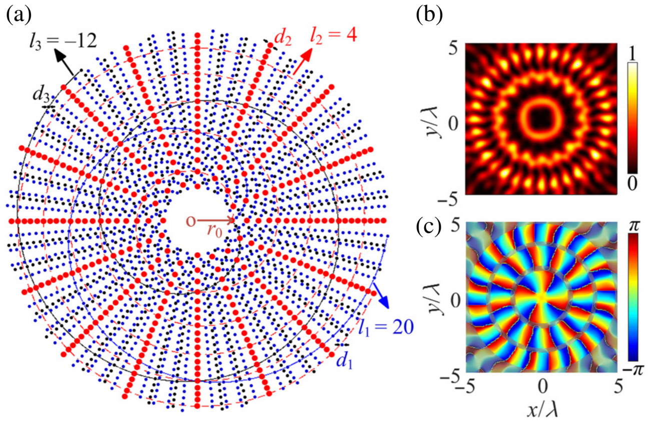

FIG. 6. (a) Schematic diagram of a HDCP for generating a triple-ring FAV with $l_1 = 20$, $l_2 = 4$, and $l_3 = -12$. Here, d_1, d_2, and d_3 are 0.7 mm, 2.1 mm, and 0.7 mm, respectively. Corresponding (b) normalized simulated acoustic intensity and (c) phase distributions of the transmitted acoustic fields at the focal plane of $z = 20\lambda$. The work frequency is 500 kHz and the embedding medium is water.

distributions. Figure 7(c1) displays simulated (the black solid line) and measured (the red dotted-dashed line) intensity profiles along the white dashed lines in Figs. 7(a1) and 7(b1). Figure 7(c2) shows simulated (the black solid line) and measured (the red dotted-dashed line) phase

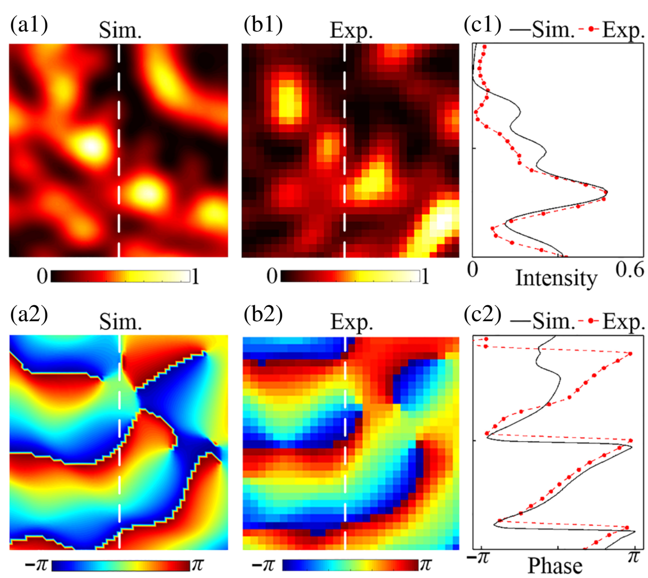

FIG. 7. (a1) Normalized simulated and (b1) measured acoustic intensity distributions in the measurement area. (c1) Simulated (the black solid line) and measured (the red dotted-dashed line) intensity profiles along the white dashed lines in (a1) and (b1). Corresponding (a2) simulated and (b2) measured phase distributions. (c2) Simulated (the black solid line) and measured (the red dotted-dashed line) phase profiles along the white dashed lines in (a2) and (b2).

profiles along the white dashed lines in Figs. 7(a2) and 7(b2). It is observed that the simulations and the measured results exhibit good agreement, although there are some slight deviations. These deviations may arise from fabrication imperfections in the structure, as well as the inherent limitations in the precision of the experimental system.

[1] Y. R. Jia, Y. M. Liu, B. L. Hu, W. Xiong, Y. C. Bai, Y. Cheng, D. J. Wu, X. J. Liu, and J. Christensen, Orbital angular momentum multiplexing in space–time thermoacoustic metasurfaces, Adv. Mater. **34**, 2202026 (2022).

[2] Z. Y. Sun, Y. Shi, X. C. Sun, H. Jia, Z. K. Jin, K. Deng, and J. Yang, Underwater acoustic multiplexing communication by pentamode metasurface, J. Phys. D: Appl. Phys. **54**, 205303 (2021).

[3] X. R. Li, J. J. Feng, B. C. Ping, Y. Sun, D. J. Wu, and B. Assouar, Periodic-phase acoustic vortices with tunable comblike orbital angular momentum spectrum, Phys. Rev. Appl. **20**, 034008 (2023).

[4] Y. R. Jia, S. Y. Zhang, X. Zhang, H. Y. Long, C. B. Xu, Y. C. Bai, Y. Cheng, D. J. Wu, M. X. Deng, C. W. Qiu, and X. J. Liu, Compact meta-differentiator for achieving isotropically high-contrast ultrasonic imaging, Nat. Commun. **15**, 2934 (2024).

[5] T. Li, J. L. Li, L. Y. Bo, H. Bachman, B. Fan, J. T. Cheng, and Z. H. Tian, Robot-assisted chirality-tunable acoustic vortex tweezers for contactless, multifunctional, 4-DOF object manipulation, Sci. Adv. **10**, eadm7698 (2024).

[6] Y. C. Luo, Y. R. Jia, J. Yao, D. J. Wu, and X. J. Liu, Enhanced fractional acoustic vortices by an annulus acoustic metasurface with multi-layered rings, Adv. Mater. Technol. **5**, 2000356 (2020).

[7] X. M. Ren, Q. X. Zhou, Z. Xu, and X. J. Liu, Particle trapping in arbitrary trajectories using first-order Bessel-like acoustic beams, Phys. Rev. Appl. **15**, 054041 (2021).

[8] T. Li, J. L. Li, L. Y. Bo, M. R. Brooks, Y. S. Du, B. W. Cai, Z. Pei, L. Shen, C. C. Sun, J. T. Cheng, Y. A. Pan, and Z. H. Tian, Airborne acoustic vortex end effector-based contactless, multi-mode, programmable control of object surfing, Adv. Mater. Technol. **9**, 2400564 (2024).

[9] Y. D. Ruan, J. Zhu, Q. H. Lin, Y. Q. Wang, D. K. Zhou, S. B. Wang, C. Li, J. H. Shi, and R. M. Chen, Reflective vortex focusing for acoustic contact-free object rotation, J. Sound Vib. **581**, 118380 (2024).

[10] D. C. Chen, Q. X. Zhou, X. F. Zhu, Z. Xu, and D. J. Wu, Focused acoustic vortex by an artificial structure with two sets of discrete Archimedean spiral slits, Appl. Phys. Lett. **115**, 083501 (2019).

[11] S. F. Guo, X. Y. Guo, X. Wang, X. Du, P. Y. Wu, A. Bouakaz, and M. X. Wan, Manipulation of nanodroplets via a nonuniform focused acoustic vortex, Phys. Rev. Appl. **13**, 034009 (2020).

[12] Z. G. Zou, R. Lirette, and L. K. Zhang, Orbital angular momentum reversal and asymmetry in acoustic vortex beam reflection, Phys. Rev. Lett. **125**, 074301 (2020).

[13] X. Z. Ke and L. Zhang, Study on orthogonal superposition generation method of double-ring vortex beams, Eur. Phys. J. D **74**, 45 (2020).

[14] V. Bobkova, J. Stegemann, R. Droop, E. Otte, and C. Denz, Optical grinder: sorting of trapped particles by orbital angular momentum, Opt. Express **29**, 12967 (2021).

[15] Y. F. Du, D. M. Liu, S. N. Fu, Y. C. Wang, and Y. W. Qin, Reconfigurable generation of double-ring perfect vortex beam, Opt. Express **29**, 17353 (2021).

[16] S. V. Karpeev, V. D. Paranin, and S. N. Khonina, Generation of a controlled double-ring shaped radially polarized spiral laser beam using a combination of a binary axicon with an interference polarizer, J. Opt. **19**, 055701 (2017).

[17] Z. Q. Nie, Z. G. Li, G. Shi, X. R. Zhang, Y. X. Wang, and Y. L. Song, Generation of a sub-wavelength focal spot with a long transversally polarized optical needle using a double-ring-shaped azimuthally polarized beam, Opt. Lasers Eng. **59**, 93 (2014).

[18] H. Wang, X. Liu, P. G. Jing, and Y. Liu, Airborne ultrasound haptics from amplitude and spatiotemporal modulation of acoustic vortices, IEEE Sens. Lett. **7**, 2502004 (2023).

[19] Q. D. Wang, Y. T. Hu, S. L. Wang, and H. Y. Li, Helical particle manipulation based on power-exponent-phase acoustic vortices generated by a sector transducer array, Chin. Phys. B **32**, 064304 (2023).

[20] Q. X. Zhou, X. M. Ren, J. Huang, Z. Xu, and X. J. Liu, Beam shaping in Fourier-transform acoustic systems, Phys. Rev. Appl. **20**, 024015 (2023).

[21] J. Y. Wang, X. R. Li, X. F. Zhu, J. Yao, Q. Wei, and D. J. Wu, Ultrasonic braided ring beams generated by phase modulation metasurfaces, Appl. Phys. Lett. **124**, 081703 (2024).

[22] X. R. Li, Y. R. Jia, Y. C. Luo, J. Yao, and D. J. Wu, Mixed focused-acoustic-vortices generated by an artificial structure plate engraved with discrete rectangular holes, Appl. Phys. Lett. **118**, 043503 (2021).

[23] Y. J. Yang, G. Thirunavukkarasu, M. Babiker, and J. Yuan, Orbital-angular-momentum mode selection by rotationally symmetric superposition of chiral states with application to electron vortex beams, Phys. Rev. Lett. **119**, 094802 (2017).

[24] Z. W. Jin, D. Janoschka, J. H. Deng, L. Ge, P. Dreher, B. Frank, G. W. Hu, J. C. Ni, Y. J. Yang, J. Li, C. Y. Yu, D. Y. Lei, G. X. Li, S. M. Xiao, S. T. Mei, H. Giessen, F. M. Z. Heringdorf, and C. W. Qiu, Phyllotaxis-inspired nanosieves with multiplexed orbital angular momentum, eLight **1**, 5 (2021).

[25] X. R. Li, Y. R. Jia, Y. C. Luo, J. Yao, and D. J. Wu, Coupled focused acoustic vortices generated by degenerated artificial plates for acoustic coded communication, Adv. Mater. Technol. **7**, 2200102 (2022).

[26] N. Jiménez, V. Romero-García, L. M. García-Raffi, F. Camarena, and K. Staliunas, Sharp acoustic vortex focusing by Fresnel spiral zone plates, Appl. Phys. Lett. **112**, 204101 (2018).

[27] D. C. Chen, X. Liu, D. J. Wu, X. F. Zhu, Q. Wei, Y. Cheng, and X. J. Liu, Acoustic spin-controlled orbital rotations in double spiral acoustic beams, Commun. Phys. **7**, 212 (2024).

[28] Y. C. Luo, X. R. Li, D. J. Wu, J. Yao, X. F. Zhu, L. F. Du, and X. J. Liu, Three-dimensional trapping and manipulation of a Mie particle by hybrid acoustic focused petal beams, Phys. Rev. Appl. **17**, 064059 (2022).

[29] Y. C. Luo, X. R. Li, X. F. Zhu, J. Yao, and D. J. Wu, Acoustic dark lattices generated by composite spiral plates for multiparticle trapping, Appl. Acoust. **211**, 109529 (2023).

[30] K. Melde, A. G. Mark, T. Qiu, and P. Fischer, Holograms for acoustics, Nature **537**, 518 (2016).

[31] B. Hartmann and J. Jarzynski, Immersion apparatus for ultrasonic measurements in polymers, J. Acoust. Soc. Am. **56**, 1469 (1974).